Langmuir

Article

pubs.acs.org/Langmuir

Molecular Dynamics Study of Nanoconfined Water Flow Driven by Rotating Electric Fields under Realistic Experimental Conditions

Sergio De Luca,[†] B. D. Todd,*[,†] J. S. Hansen,[‡] and Peter J. Daivis[¶]

[†]Department of Mathematics, Faculty of Science, Engineering and Technology, and Centre for Molecular Simulation, Swinburne University of Technology, Melbourne, Victoria 3122, Australia

[‡]DNRF Center 'Glass and Time', IMFUFA, Department of Science, Systems and Models, Roskilde University, DK-4000 Roskilde, Denmark

[¶]School of Applied Sciences, RMIT University, Melbourne, Victoria 3001, Australia

ABSTRACT: In our recent work, *J. Chem. Phys.* **2013**, *138*, 154712, we demonstrated the feasibility of unidirectional pumping of water, exploiting translational−rotational momentum coupling using nonequilibrium molecular dynamics simulations. Flow can be sustained when the fluid is driven out of equilibrium by an external spatially uniform rotating electric field and confined between two planar surfaces exposing different degrees of hydrophobicity. The permanent dipole moment of water follows the rotating field, thus inducing the molecules to spin, and the torque exerted by the field is continuously injected into the fluid, enabling a steady conversion of spin angular momentum into linear momentum. The translational−rotational coupling is a sensitive function of the rotating electric field parameters. In this work, we have found that there exists a small energy dissipation region attainable when the frequency of the rotating electric field matches the inverse of the dielectric relaxation time of water and when its amplitude lies in a range just before dielectric saturation effects take place. In this region, that is, when the frequency lies in a small window of the microwave region around ∼20 GHz and amplitude ∼0.03 V Å^{-1}, the translational−rotational coupling is most effective, yielding fluid velocities of magnitudes of ∼2 ms^{-1} with only moderate fluid heating. In this work, we also confine water to a realistic nanochannel made of graphene giving a hydrophobic surface on one side and β-cristobalite giving a hydrophilic surface on the other, reproducing slip-and-stick velocity boundary conditions, respectively. This enables us to demonstrate that in a realistic environment, the coupling can be effectively exploited to achieve noncontact pumping of water at the nanoscale. A quantitative comparison between nonequilibrium molecular dynamics and analytical solutions of the extended Navier−Stokes equations, including an external rotating electric field has been performed, showing excellent agreement when the electric field parameters match the aforementioned small energy dissipation region.

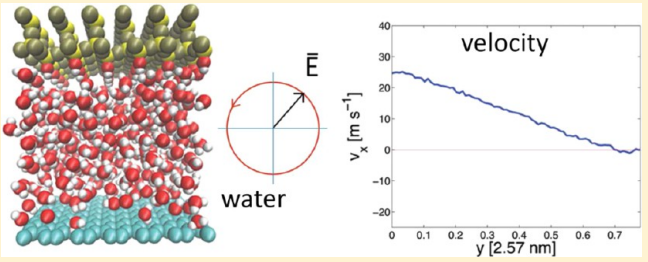

INTRODUCTION

In the broad field of nanotechnology, nanofluidics has achieved a privileged position, with potentially vital applications such as the removal of toxic inorganic species from water,[1] desalination,[1,2] and cell biology.[3] Moreover, the interest aroused by the exceptional properties of nanoflow conduits like graphene and carbon nanotubes,[4−6] provides even more stimulation for its rapid progress.

Flow manipulation at the nanoscale can be achieved by applying external forces on the fluid, such as pressure gradients or electric fields as in electroosmotic flow.[7] Modern approaches include diffusio-osmosis,[8] vibrating carbon nanotubes,[9] and temperature gradients.[10] Specific charge distributions on carbon nanotubes mimicking the membrane acquaporin,[11] or polarization drag effects,[12] are examples of recent advances exploiting the electric field, which dominates at the nanoscale level.

Recently, a noncontact methodology to pump water at the nanoscale has been proposed,[13,14] which does not require external mechanical intervention or charge injection into the fluid. Its theoretical foundation, which relies upon the coupling between linear streaming momentum and the intrinsic angular momentum,[15−18] has been established,[13,14,19−25] and the first nonequilibrium molecular dynamics (NEMD) experiment demonstrating its feasibility has been only recently carried out.[26] Two conditions must be satisfied to attain a net flow rate production. First, a spatially uniform rotating electric field (REF) acts on the polar fluid.[13,14,19,26] The water molecule has an asymmetric partial charge distribution giving rise to a permanent dipole moment. A uniform electric field cannot exert a net force on the center of mass of a water molecule, but it exerts a torque that rotates the dipoles. Owing to the intermolecular interactions, the excited rotations enable conversion of spin angular momentum into streaming linear momentum. Second, the fluid must be confined between surfaces with different degrees of hydrophobicity to reproduce

Received: December 23, 2013
Revised: February 18, 2014
Published: February 27, 2014

   dx.doi.org/10.1021/la404805s | *Langmuir* 2014, 30, 3095−3109

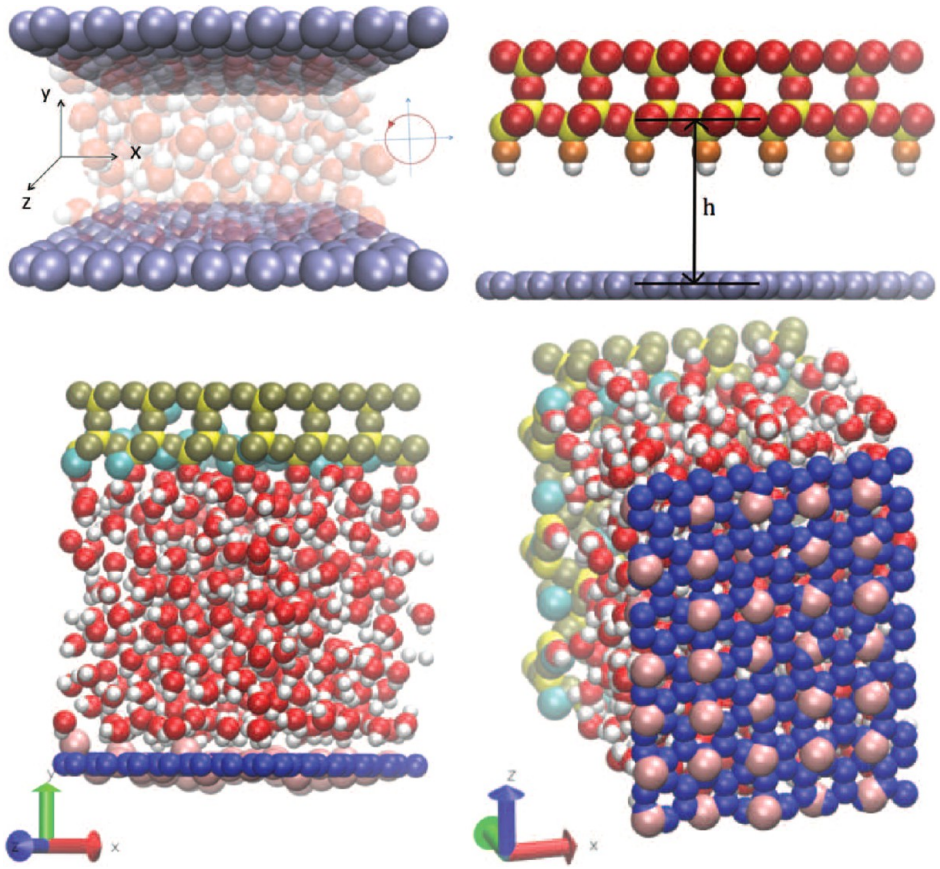

Figure 1. (top left) Perspective view of the symmetric system (i.e., composed of two graphene sheets). Partially transparent water molecules are depicted between the walls. (top right) Ortographic view of the asymmetric system (i.e., graphene and β-cristobalite), rotated around the y axis by 45°. Nonbridging oxygens (nbO) are orange, bridging oxygens (bO) red, and silica yellow. The nbO are saturated with hydrogen (white). The distance h represents the center of mass separation between the two walls. The red circle (top left) shows the direction of rotation of the external electric field, lying on the x–y plane. (bottom left) Water molecules confined between graphene and β-cristobalite. The carbon atoms of the graphene sheet are colored in blue and the atoms of β-cristobalite are colored in yellow (silica) and dark green (bridging oxygens). The silanol–SiOH groups (bonded to the innermost silica atoms) are colored in white (hydrogen) and red (nonbridging oxygens). The virtual particles of the VP thermostat are colored in light blue and pink. (bottom right) Top-bottom view of the same system which shows the rectangular grid of the virtual particles.

the asymmetric boundary conditions (BC) required by the fluid to attain a net flow production. In molecular dynamics, asymmetric BCs can be implemented with walls having different wetting characteristics, to provide the stick-and-slip velocity BC at the hydrophilic and hydrophobic interfaces, respectively. However, implementing a symmetric BC (i.e., confining water between two identical planar walls) results in a zero net flow, although some characteristics of the fluid dynamics are preserved, as will be detailed later.

In our previous work,[26] we performed NEMD simulations of water molecules confined between highly idealized surfaces. Applying a REF with frequencies ≈20 GHz and high field strengths ≈0.2 V Å^{-1}, fluid velocities ≈50 ms^{-1} were obtained. We reported a qualitative agreement with the extended Navier–Stokes equations (ENS), which were also solved numerically in the steady state taking the velocity and angular velocity BC from NEMD simulation data.

In this work, we use realistic surfaces to reproduce the stick-and-slip velocity BC near the interfaces. Moreover, since the ENS were solved under the assumption that the system is in the linear regime,[14] we employ a lower range of REF amplitudes than the one used by De Luca et al.[26] and the lowest value of this range will be used in the last section as a reference value to compare theory with NEMD simulations. Our aim in this work is to demonstrate by computer simulations that an actual physical experiment of such a system using realistic material channels is feasible.

■ SIMULATIONS

We employ NEMD techniques with code developed by the authors. The first objective of our investigation is to measure fluid velocities when realistic walls confine water molecules, in particular, implementing the symmetric channels composed of two equal hydrophobic walls and the asymmetric channels composed of one hydrophilic and one hydrophobic surface. Confining surfaces are selected according to their ability to reproduce stick-and-slip velocity boundary conditions at the wall–water interface. Silica materials and carbon-based structures may be used as hydrophilic and hydrophobic walls, respectively. We select β-cristobalite SiO_2, whose structure,[27] water adsorption characteristics, and strong hydrophilicity have been investigated.[28,29] The Si atoms of β-cristobalite form the diamond structure with a cubic unit cell of 0.716 nm size. Each Si is surrounded by four oxygens arranged in a tetrahedron with bond angles of 109.47°. The network is cut along the (111) plane and the unsaturated oxygens were hydroxylated with

dx.doi.org/10.1021/la404805s | Langmuir 2014, 30, 3095–3109

hydrogen atoms at the distance of 1 Å from the oxygen, perpendicular to the surface.[29] Note that two different (111) Miller planes may be chosen, depending on the distance between the cut plane and a fixed reference point, thus giving two possible silanol (−SiOH) surface densities, 4.54 or 13.53 OH/nm^2.[29] We selected 4.54 OH/nm^2, since this density is close to experimental surface charge densities for silica.[30]

The electric field performs work on the fluid, enhancing viscous friction between fluid elements. The fluid temperature increases and heat must be removed to attain the steady state. To absorb heat excess from the fluid, we use a new thermostat (so-called virtual particle scheme, or VP scheme) devised and tested by us[31] and suitable for nanoconfined fluids. This scheme allows us to avoid a direct application of the thermostat on the fluid molecules, enabling heat to be naturally conducted from the fluid through the surface, as happens in a real experiment. Moreover, walls can be kept rigid, thus improving the system stability and saving computational time since they are not thermalized. When frozen walls are implemented, it is customary in MD to apply a thermostat directly to the fluid. However, this may lead to unphysical results.[32] If the fluid is not coupled with a thermostat, a thermal wall is usually implemented, in which the walls' atoms vibrate around their equilibrium lattice positions and absorb the excess heat by means of their interactions with the fluid, at a rate which depends on the stiffness of the spring constant. When a complex and charged surface such as β-cristobalite confines a polar fluid such as water, a reasonable value of the spring constant which imparts stability, simultaneously enabling efficient thermal transport through the walls, may be difficult to obtain. We have verified that when water is exposed to the aforementioned β-cristobalite surface and immersed in external electric fields of the order used in this work, a very high spring constant value is required to preserve wall stability, which is reduced by the strong Coulomb interactions between water and the charged surface. This leads to atomic vibrational frequencies which degrade the thermostatting performance. Our thermostatting strategy[31] enables a frozen β-cristobalite wall to coexist with unthermostatted fluids. Thus, we bypass the risk that a synthetic thermostat applied to the fluid may interfere with the fluid dynamics, simultaneously enhancing system stability and avoiding permeation of water molecules through the surface. The thermostatting functionality is performed by the so-called virtual particles (VP) located close to the walls, which vibrate and interact only with the fluid molecules, absorbing the heat excess.

A schematic diagram of the surface is plotted at the bottom left of Figure 1 where β-cristobalite is positioned parallel to the $x-z$ plane. A snapshot of the system which also shows the VPs is plotted at the bottom right of Figure 1. The Lennard−Jones parameters for the silica surface were taken from Argyris et al.[29] who examined static and dynamics properties of the SPC/E water model[33] (also used by us) in contact with the (111) crystallographic face of β-cristobalite. Following their nomenclature, that is, indicating the bridging oxygen as bO (shared by two SiO_4 tetrahedra) and the nonbridging oxygen as nbO (bonded to one Si atom), we fix ε_{bO} = 1.1911 kJ/mol, σ_{bO} = 0.27 nm, $q_{nbO} = -0.533e$ ($e = 1.6 \times 10^{-19}$ C is the fundamental unit of charge), ε_{nbO} = 1.1911 kJ/mol, σ_{nbO} = 0.3 nm, $\varepsilon_{Si} = 0$, $\sigma_{Si} = 0$, $q_{Si} = 1.283e$, $\varepsilon_H = 0$, $\sigma_H = 0$, and $q_H = 0.206e$. Note that to preserve the electroneutrality of the whole system, we do not use $fq_{bO} = -0.629e$[29] or the partial charge of the bO oxygen, but we made a small correction to this value using $q_{bO} = -0.587e$.

A sheet of graphene,[34] a hexagonal lattice of carbon atoms with bond length 0.142 nm positioned parallel to the $x-z$ plane, represents the hydrophobic wall (top left of Figure 1). The graphene is kept rigid for the reasons explained before, regarding the rigidity of β-cristobalite. The Lennard−Jones interaction potential parameters between the water's oxygen and carbon are ε_{CO} = 0.392 kJ/mol and σ_{CO} = 0.319 nm.[35] We consider two graphene sheets to represent the symmetric channel and a sheet of graphene opposite to a slab of β-cristobalite for the asymmetric channel.

The simulation box dimensions for the asymmetric channel are L_x = 2.02 nm, L_y = 6.55 nm, and L_z = 2.63 nm, and for the symmetric channel, L_x = 1.97 nm, L_y = 6.37 nm, and L_z = 2.13 nm, both periodic in the x and z directions. For the asymmetric channel, the lattice constants of graphene and β-cristobalite cannot simultaneously satisfy the same periodic boundary conditions in the x and z directions, hence, to match their crystal lattices in the simulation box, we distort the graphene sheet by ∼7% in the x direction and ∼3% in the z direction. In the study of the stability of graphene on a SiO_2 surface, distortions of ∼5% have been applied to correct for their lattice constant mismatch.[36] We have verified that simulating Poiseuille flow, employing graphene and its deformed version yields approximately equal slip velocities at the interface.

We use the rigid nonpolarizable SPC/E water model[33] with SHAKE[37] constraining the O−H water bond length at 0.1 nm and the H−O−H angle at 109.5°. The partial charges q_H = 0.4238e and $q_O = -0.8476e$ reside on the hydrogen and oxygen atoms of SPC/E, respectively, giving the permanent dipole moment 2.35 D, in agreement with the experimental value of 2.9 ± 0.6 D.[38] The interaction between water molecules is modeled through the pairwise additive Lennard−Jones (LJ) potential and point charge Coulomb interaction between atoms making up the water molecules

$$\phi_{ij} = \sum_i \sum_{j>i} 4\varepsilon_{ij}\left[\left(\frac{\sigma_{ij}}{r_{ij}}\right)^{12} - \left(\frac{\sigma_{ij}}{r_{ij}}\right)^{6}\right] + \sum_i \sum_{j>i} \frac{q_i q_j}{4\pi\varepsilon_0 r_{ij}} \quad (1)$$

where the first term in parentheses represents the short-range repulsive part and the second term models the dipole-induced attractive part. The Coulomb term describes the electric interactions between charged sites of different molecules, computed with the Wolf algorithm[39] with a cutoff truncation radius of 0.918 nm. The Wolf method (which is a cut and shifted method) may induce a spurious electric field in confined systems.[40,41] To investigate the magnitude of the fictitious field induced by this method, we calculated the charge density profile based on the atomic charges. Using the Poisson equation for electrostatics, one can evaluate the electric potential and thus the electrical field profile. Near the walls the field is rapidly varying due to alignment of the water molecules, but in the bulk it should be zero.[40] In our system, we observe a maximum fictitious field away from the wall of around 0.003 V Å^{-1}, which is 1 order of magnitude smaller than the lowest external field amplitude applied. We therefore do not expect this to have significant effects on results. We also test whether the calculation of electrostatic interactions in the inhomogeneous fluid with the Wolf method had a strong effect, computing the viscosity by fitting the velocity profile for Poiseuille flow simulations driven by an applied gravitational

dx.doi.org/10.1021/la404805s | Langmuir 2014, 30, 3095−3109

field, with no applied electric field. The value of the viscosity obtained by extrapolating to a zero external gravitational field was $(6.9 \pm 0.4) \times 10^{-4}$ Pas, marginally higher than the value of $(6.5 \pm 0.5) \times 10^{-4}$ Pas obtained using the Green−Kubo formula from independent homogeneous equilibrium simulations on a 500 molecule system (using the full Ewald method) at the same state point (found by extrapolating the average temperature of the Poiseuille flow simulations to the zero field limit, giving T = 311 K and ρ = 998 kg m^3). Note that translational−rotational coupling can also affect the velocity profile obtained from Poiseuille flow simulations on molecules with a nonzero moment of inertia, reducing the flow rate. This is consistent with the slightly higher value of the effective viscosity found here when the coupling is ignored. These values are in good agreement with $(7.13 \pm 0.1) \times 10^{-4}$ Pas obtained at T = 298 K[42] and with $(6.63 \pm 0.239) \times 10^{-4}$ Pas at T = 303 K.[43] The constant ε_{ij} which represents the depth of the LJ potential, is employed as an energy scale parameter, while σ_{ij}, the particle distance at which $\phi_{ij} = 0$, is used as a length scale parameter; $\varepsilon_0 = 8.854 \times 10^{-12}$ Fm^{1-} is the vacuum permittivity. The distance between two sites of different molecules is $r_{ij} = |\mathbf{r}_i - \mathbf{r}_j|$, where $\mathbf{r}_i$ and $\mathbf{r}_j$ are the position vectors of the oxygen and/or hydrogen sites of water, and the graphene, β-cristobalite atoms, or the virtual particles. Note that the virtual particles interact only with the water's oxygens and not with the wall atoms. The mass scaling factor corresponds to the mass of the oxygen $m_O = 2.66 \times 10^{-26}$ kg with the virtual particle mass $m_{VP} = m_O$. For oxygen−oxygen interactions, we used the SPC/E Lennard−Jones parameters ε = 0.6502 kJ/mol (energy scaling factor) and σ = 0.3166 nm (length scaling factor), and for hydrogen−hydrogen and oxygen−hydrogen, they are 0. The interactions between water and graphene are represented only by the LJ term, since graphene is considered neutral and r_{ij} in this case indicates the distance between oxygen and carbon sites. Equation 1 also models LJ interactions between water's oxygen and bO and nbO sites, and the Coulomb interactions between water and β-cristobalite charged atoms, with LJ parameters and partial charges as explained. The water's oxygen also interacts with the virtual particles. We fix $\varepsilon_{wVP} = \varepsilon$ and $\sigma_{wVP} = \sigma$ for the Lennard−Jones interaction between virtual particles and water. All the LJ interactions are truncated at $r = 2.5\sigma_{ij}$, where σ_{ij} are evaluated with the Lorentz−Berthelot mixing rules. The density of water is fixed at ρ = 998 kgm^{-3} for the systems considered.

The separation between the walls is h = 2.57 nm for the symmetric channel and the asymmetric channel and corresponds to the distance between the center of mass of the two graphene sheets (for the symmetric channel) and the distance between the center of mass of the graphene sheet and the center of mass of the innermost (closest to the fluid) bO β-cristobalite layer (for the asymmetric channel), denoted with h in Figure 1, top right. The walls are positioned symmetrically with respect to the center of the simulation box along the y direction with $L_y \lesssim 3h$. To estimate the accessible volume for water inside the symmetric channel, we consider an effective distance between the walls obtained by subtracting from h = 2.57 nm the segment σ_{CO}, which accounts for the excluded region next to the interfaces due to the repulsive part of the LJ interactions. Hence, the number of water molecules in the symmetric channel is $N_w = \rho L_y' L_x L_z / m_w$, where $L_y' = h - \sigma_{CO}$ and m_w is the water mass. For the asymmetric channel, we subtract $\sigma_{CO}/2$, which accounts for the graphene exclusion layer and $\sigma_{ObO}/2$ for the innermost bO layer of β-cristobalite. Again $N_w = \rho L_y' L_x L_z / m_w$, where $L_y' = h - (\sigma_{ObO} + \sigma_{CO})/2$, except now we subtract one water molecule for every SiOH surface silanol group. Note that the distance between one nbO and the center of mass of the innermost bO plane is ≃2 Å, and the intersilanol group distance is ≃5 Å. We have checked equilibrium density profiles, verifying that for N = 375 water molecules with the asymmetric channel and for N = 314 with the symmetric channel, the expected bulk densities were attained in the central region of the channel.

To drive the flow out of equilibrium we apply a REF represented by the time-dependent vector field $\mathbf{E} = E[\cos(2\pi\nu t), \sin(2\pi\nu t), 0]$, where E and ν are the REF amplitude and frequency. The field rotates in the x−y plane, as depicted in Figure 1, top left. The torque exerted on a single water molecule is

$$\tau = \sum_i (\mathbf{r}_i - \mathbf{r}_{cm}) \times q_i \mathbf{E}_i \tag{2}$$

where i indexes the hydrogen and oxygen atomic sites located at $\mathbf{r}_i$, q_i are the partial charges, and $\mathbf{r}_{cm}$ is the center of mass. The torque attempts to align the permanent dipole moment in the REF direction, increasing its average angular velocity in the z direction. This alignment is counteracted by the intermolecular forces acting between molecules, by the thermal energy which reverts the dipoles to random orientations, and by the interfaces which hinder the dipoles' ability to follow the field. Only the orientational polarization mechanism is involved since SPC/E is rigid and nonpolarizable. It is important to note that we neglect any quantum and chemical reaction effect; in particular, we do not explicitly account for atomic or electronic polarization effects (thus neglecting the charge transfer mechanism), since the proposed pumping method and the hydrodynamic theory (with which we compare our NEMD results in the last section) rely upon the orientational polarization mechanism. We examine the REF amplitude range of 0.01−0.15 V Å^{-1} and frequency in the microwave region 20−300 GHz, which provide significant fluid velocities in the accessible simulation time of 10−20 ns, without excessive heating of water (when the frequency is not too high). These field magnitudes are comparable to those used in NEMD studies of microwave heating of water, in which a large fluid heating is detected with 100 GHz and 0.1 V Å^{-1}[44] and a temperature increase of 50 K (after the initial T = 300 K) with 10 GHz and 0.02 V Å^{-1}.[45]

The Newtonian equations of motion for the atoms comprising water molecules with the inclusion of REF are

$$\dot{\mathbf{r}}_i = \frac{\mathbf{p}_i}{m_i} \tag{3}$$

$$\dot{\mathbf{p}}_i = \mathbf{F}_i + q_i \mathbf{E}_i \tag{4}$$

where $\mathbf{E}_i$ is the electric field acting on atom i, m_i the mass, q_i the partial charge, and $\mathbf{p}_i$ the laboratory momentum of atom i. $\mathbf{F}_i$ represents the total intermolecular force acting on atom i due to all other atoms and the forces exerted by the thermostat.[31] Eqs 3 and 4 are integrated with the leapfrog method,[46] with a time step of Δt = 1.57 fs.

Water molecules are arranged at the beginning of the simulation in a rectangular grid such that the oxygens do not overlap. The particles performing the thermostatting functionality are distributed next to graphene and β-cristobalite and the temperature of the thermostat is fixed at T = 298 K.[31] During the first 2×10^5 time steps, the system equilibrates and then the

dx.doi.org/10.1021/la404805s | Langmuir 2014, 30, 3095−3109

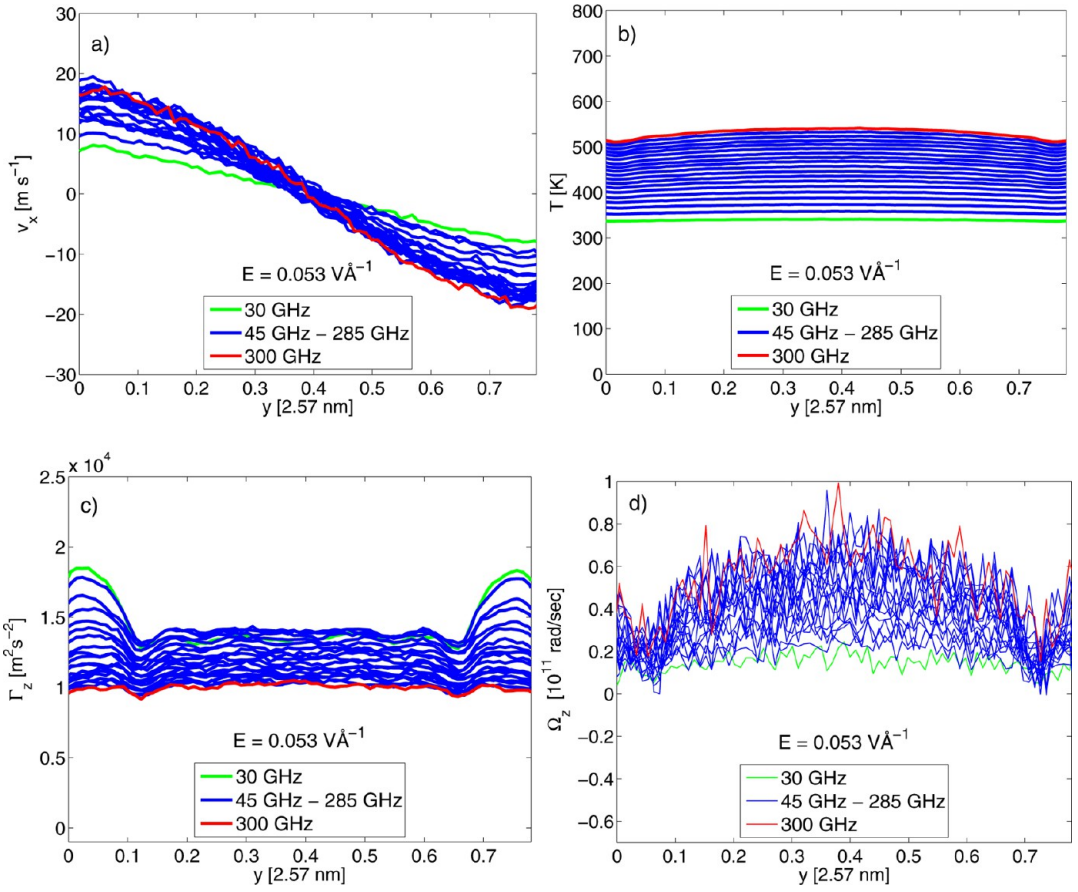

Figure 2. (a) Streaming velocity profiles of water confined between two graphene layers (symmetric channel), with fixed electric field amplitude and varying frequency (values on top and inside the legend, respectively). The horizontal axis (y coordinate of the simulation box) represents the graphene−graphene center of mass distance. (b) Temperature profiles of water. (c) Specific torque profiles. (d) Streaming angular velocity profiles. The horizontal axis represents the width $h' \lesssim h_{\text{eff}} \simeq 0.80 \times 2.57$ nm $\simeq 2$ nm.

REF is switched on, allowing a further 6×10^6 time steps to reach the steady state. Time averages of properties of interest such as density, streaming velocity, streaming angular velocity, specific torque, and temperature profiles, are accumulated during the successive 8×10^6 time steps. Profiles are collected by sampling every 10 time steps and employing standard binning techniques[46] with 101 bins of $\Delta y = 0.25$ Å size.

The streaming velocity $v_x(y)$, where x denotes the flow direction and y the vertical direction (see Figure 1), has been computed by means of the microscopic definition of the momentum flux density

$$J_x(y, t) = \frac{1}{L_x L_z} \sum_i m_i v_{x,i} \delta(y - y_i) \tag{5}$$

divided by the mass density

$$\rho(y, t) = \frac{1}{L_x L_z} \sum_i m_i \delta(y - y_i) \tag{6}$$

where i indexes the water molecule, m_i is the mass of water, $v_{x,i}$ is the x velocity component of the ith water molecule, and y_i is the center of mass of molecule i. Profiles are averaged over the x and z coordinates on slabs defined by the two vertical coordinates y and $y + \Delta y$, where y spans the width of the channel (i.e., from 0 to 2.57 nm). When the simulation ends, the streaming velocity is obtained computing

$$v_x(y) = \frac{\langle \sum_i m_i v_{x,i} \delta(y_i - y) \rangle}{\langle \sum_i m_i \delta(y_i - y) \rangle} \tag{7}$$

evaluated for every bin. The angle brackets represent time averages over 8×10^6 time steps in the steady state. With the same binning technique, we compute the molecular center of mass kinetic temperature

$$T_{\text{m}} = \frac{1}{3 N_{\text{w}} k_{\text{B}}} \sum_i m_i \mathbf{c}_{i,\text{cm}}^2 \tag{8}$$

where $\mathbf{c}_{i,\text{cm}}$ is the thermal velocity of the center of mass of molecule i, meaning that the streaming velocity contribution, eq 7, is subtracted out.

The specific torque (torque per unit mass) injected into the fluid by the REF is computed by binning the z component of the torque, eq 2, for instance, evaluating

$$\Gamma_z(y, t) = \frac{\langle \sum_i \sum_j ((x_{ij} - x_{i,cm}) q_{ij} E_{iy}(t) - (y_{ij} - y_{i,cm}) q_{ij} E_{ix}(t)) \delta(y_i - y) \rangle}{\langle \sum_i m_i \delta(y_i - y) \rangle} \tag{9}$$

where the index i counts the water molecules and j indexes the three charged sites of the SPC/E model. The term x_{ij} is the x coordinate of site j of molecule i and the term $x_{i,\text{cm}}$ is the x component of the center of mass position of molecule i, both evaluated with respect to the simulation box reference frame.

dx.doi.org/10.1021/la404805s | Langmuir 2014, 30, 3095−3109

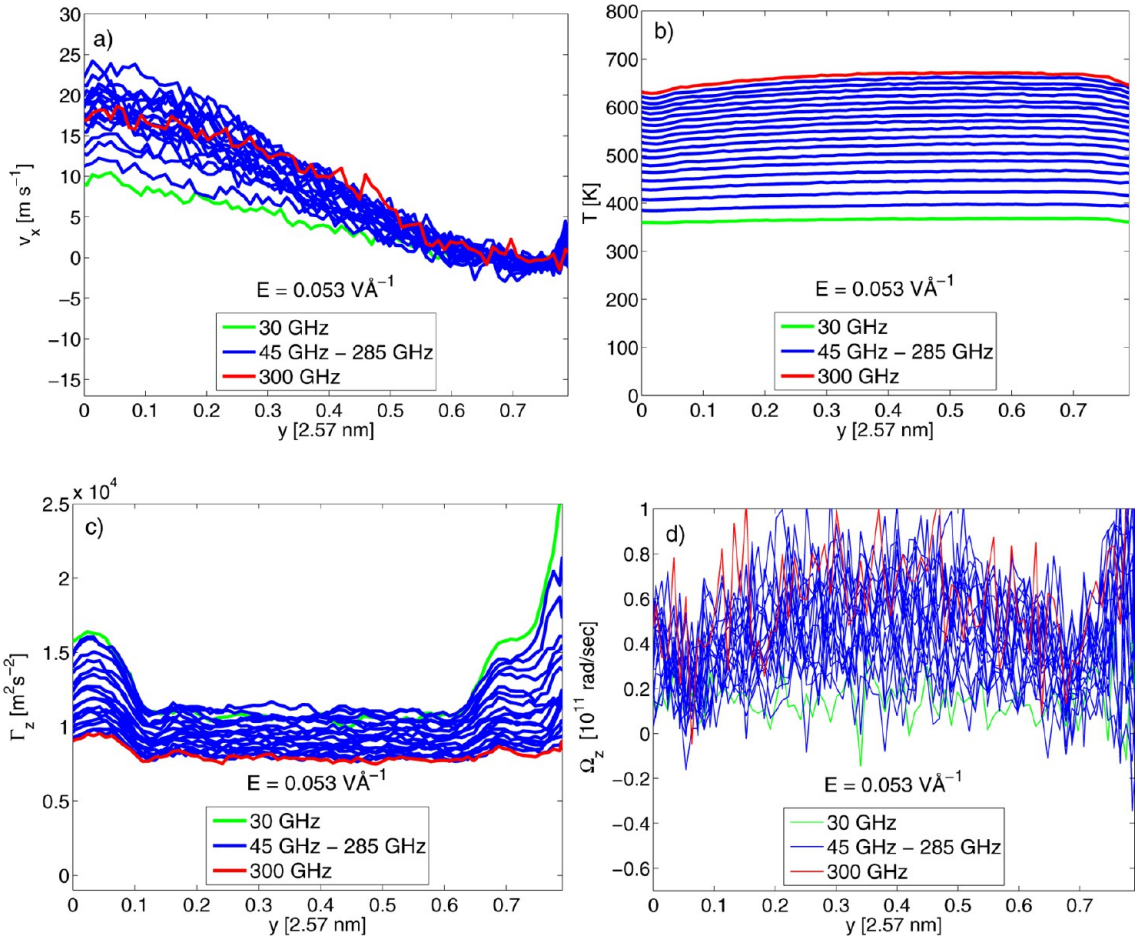

Figure 3. (a) Streaming velocity profiles of water confined between the graphene layer, located at the left (hydrophobic) side of the channel, and the (111) Miller plane of β-cristobalite is on the right (hydrophilic) side (asymmetric channel). The electric field amplitude is fixed (on top of the legend), and the frequency varies in the range indicated inside the legend. The horizontal axis (y coordinate of the simulation box) represents the distance between the graphene center of mass and the innermost (nearest to the fluid) bO layer of β-cristobalite (as detailed in Simulations). (b) Temperature profiles of water. (c) Specific torque profiles. (d) Streaming angular velocity profiles. The horizontal axis represents the width $h' \lesssim h_{\text{eff}} \simeq 0.80 \times 2.57$ nm $\simeq 2$ nm.

The terms $E_{ix}(t)$ and $E_{iy}(t)$ represent the REF x and y components acting on q_{ij}, the partial charge of site j of molecule i.

The spin angular velocity (streaming spin angular velocity) of water molecules is computed from $\mathbf{S} = \boldsymbol{\Theta}\cdot\boldsymbol{\Omega}$,[47−49] where $\mathbf{S}$, $\boldsymbol{\Theta}$, and $\boldsymbol{\Omega}$ are the specific spin angular momentum vector, moment of inertia tensor, and the streaming angular velocity vector, respectively. The intrinsic (spin) angular momentum of a water molecule is

$$\mathbf{S}_j = \sum_i (\mathbf{r}_{ji} - \mathbf{r}_{j,\text{cm}}) \times m_i(\mathbf{v}_{ji} - \mathbf{v}_{j,\text{cm}}) \tag{10}$$

where i indexes the three sites of water molecule j, $\mathbf{r}_{ji}$ represents the sites' vector position, $\mathbf{v}_{ji}$ the sites' velocity, $\mathbf{r}_{j,\text{cm}}$ the center of mass position, $\mathbf{v}_{j,\text{cm}}$ the center of mass velocity, and m_i the mass of the hydrogen and oxygen. We compute the specific spin angular momentum

$$\mathbf{S}(y) = \frac{\langle \sum_j \mathbf{S}_j \delta(y_j - y)\rangle}{\langle \sum_j m_j \delta(y_j - y)\rangle} \tag{11}$$

and the specific moment of inertia

$$\boldsymbol{\Theta}(y) = \frac{\langle \sum_j \boldsymbol{\Theta}_j \delta(y_j - y)\rangle}{\langle \sum_j m_j \delta(y_j - y)\rangle} \tag{12}$$

where j denotes water molecules with center of mass located between y_i and $y_i + \Delta_i$, $\boldsymbol{\Theta}_j$ is the moment of inertia of the molecule j, and the angle brackets refer to time averages. At the end of the simulation, we solve the linear system

$$\mathbf{S}(y) = \boldsymbol{\Theta}(y)\cdot\boldsymbol{\Omega}(y) \tag{13}$$

for Ω thus obtaining the streaming angular velocity profile across the channel.[47−49] The accuracy of the procedure can be tested[26] in a standard steady-state Poiseuille flow (flow in the x direction and planar walls laying on the x−z plane with vertical y direction), where for sufficiently wide channels (such that the spin diffusion can be neglected), the streaming angular velocity is $\Omega_z = -\dot{\gamma}/2$, where $\dot{\gamma}$ is the strain rate.

In the next section, we provide estimates of the mechanical properties of water when subjected to the REF, displaying the density (eq 6), streaming velocity (eq 7), temperature (eq 8), specific torque (eq 9), and the streaming angular velocity (eq 13), and show that the asymmetric channel must be used as a mechanism for pumping polar fluids, in accord with theory. We will further investigate the effect of varying the frequency and

dx.doi.org/10.1021/la404805s | Langmuir 2014, 30, 3095−3109

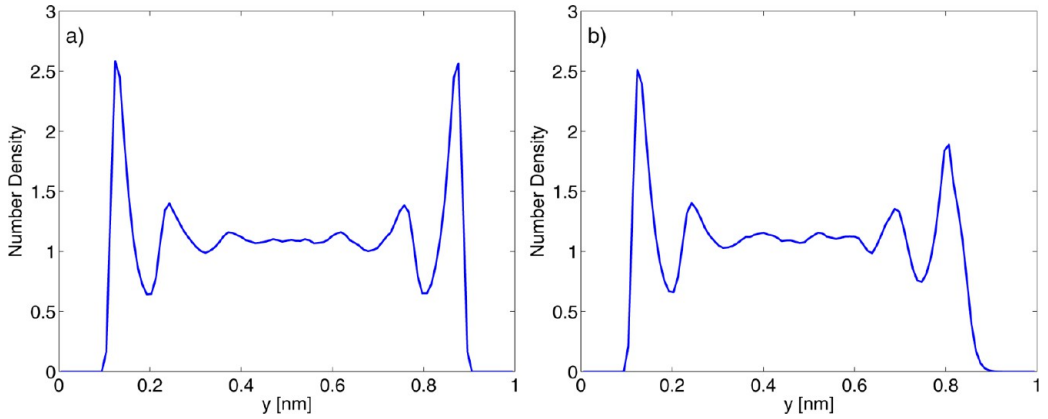

Figure 4. (a) Equilibrium density profile of water confined between two graphene layers and (b) between graphene (left side of the channel) and β-cristobalite (right side).

amplitude of the REF, highlighting several aspects of the electrokinetic flow. Some of the results presented are also preparatory for the discussion of the last section, where a quantitative comparison between our NEMD velocity profiles and the ENS predictions will be carried out.

RESULTS AND DISCUSSION

In Figure 2, we plot NEMD profiles for the symmetric channel considering nineteen REF frequencies in the range 30−300 GHz and keeping the REF amplitude fixed at E = 0.053 V Å^{-1}. All the simulations carried out are independent. Figure 2a shows the streaming velocity profiles. We observe a gradual increase of the slope of the velocity profile as the frequency increases from ν = 30 GHz (green line) to 300 GHz (red line). Profiles are approximately linear across the channel and symmetric with respect to the center (y_0 = 1.28 nm), where $v_x(y_0) \sim 0$. For ν = 30 GHz, we observe a significant slip velocity $v_x \sim 9$ ms^{-1} near the interface. Higher frequencies increase the average rotation of the permanent dipoles, and higher fluid velocities can be attained in consequence of the enhanced translational−rotational coupling. However, the trend is nonlinear and tends to saturate at higher frequencies, as will be clarified. Integrating the streaming velocity profile across the y axis yields the net flow rate production, which is found to be zero since the profile is symmetric with respect to the center of the domain of integration. Thus the symmetric channel cannot be used as a pumping mechanism for unidirectional flow. The large uncertainty in the velocity profile close to the boundaries is due to the statistical noise of the signal in those bins where a small number of water molecules is accumulated during the simulation. Figure 2b shows the temperature profiles. The lowest temperature, $T \sim 340$ K, is obtained with the lowest frequency, ν = 30 GHz, and $T \sim 530$ K is obtained when ν = 300 GHz. As the frequency increases, the number of molecular rotations per unit time increases, enhancing friction between dipoles and dissipating more heat. Figure 2c illustrates the z component of the specific torque Γ_z exerted by the REF on water. Profiles are flat in the central part of the channel, increasing (for every frequency) close to the interfaces since interactions with wall atoms impede water in its attempt to align with the field. As the frequency increases, the torque gradually decreases toward its lowest value $\Gamma_z \sim 10^4$ m^2 s^{-2} at the highest frequency, ν = 300 GHz, due to the temperature increase. That is, the thermal energy competes against the REF alignment effect, tending to randomize the dipole orientations. Finally, we illustrate in Figure 2d the streaming angular velocity profile Ω_z of water. From the lowest frequency ν = 30 GHz (green profile) to the highest ν = 300 GHz (red profile), Ω_z (taken approximately at the center of the channel) gradually increases from $\sim 0.2 \times 10^{11}$ rad/s up to $\sim 0.6 \times 10^{11}$ rad/s, since the dipoles attempt to keep up with the faster rotation of the field.

Next we examine the asymmetric channel system (see schematic in Figure 1, top right), applying field frequencies in the range of 30−300 GHz and fixing E = 0.053 V Å^{-1}, as with the symmetric channel. Figure 3a shows the streaming velocity profiles of water. On the right side of the channel, where β-cristobalite resides, the stick velocity BC is almost exactly reproduced. In other words, all the velocity profiles extrapolate to $v_x(y) \sim 0$ at the β-cristobalite side. On the opposite graphene surface, the slip velocity is $v_x \sim 11$ ms^{-1}, when ν = 30 GHz and $v_x \sim 20$ ms^{-1} when $\nu \lesssim 300$ GHz. Contrary to the symmetric channel, the integral of the velocity profile across the channel is always a positive quantity, demonstrating that the asymmetric channel enables unidirectional pumping of water. Again, the dependence of the velocity on the frequency is nonlinear and saturates at the highest frequencies, as we will see more clearly in what follows. Figure 3b displays temperature profiles illustrating a monotonic increase of the temperature from the lowest ν = 30 GHz where $T \sim 360$ K (green line) to the highest ν = 300 GHz, where $T \sim 630$ K (red line). Small asymmetries in the profiles are visible in Figure 3b with respect to the center of the channel, since different walls accommodate the same VP thermostat (with the same parameters[31]). Note that the asymmetric channel temperatures shown in Figure 3b are higher than the corresponding symmetric channel temperatures (see Figure 2b). In the symmetric channel, the slip velocities at both the graphene interfaces are different from zero (see Figure 2a at the left and right side of the channel), thus allowing a larger fraction of the energy absorbed from the REF to be converted into translational motion. On the other hand, near β-cristobalite (see Figure 3a), the dynamics of water are slowed down with fluid velocities ∼0 and a larger part of the absorbed REF energy is converted to internal kinetic energy. We further point out that for fixed E and ν, the symmetric and asymmetric channel strain rates across the channels are different. By inspecting the symmetric channel case ν = 30 GHz (see Figure 2a green profile), the strain rate is $\sim 9 \times 10^9$ s^{-1}, and for the asymmetric channel, $\sim 5 \times 10^9$ s^{-1} (see Figure 3a, green profile). Figure 3 (panels c and d) plots the specific torque and

dx.doi.org/10.1021/la404805s | Langmuir 2014, 30, 3095−3109

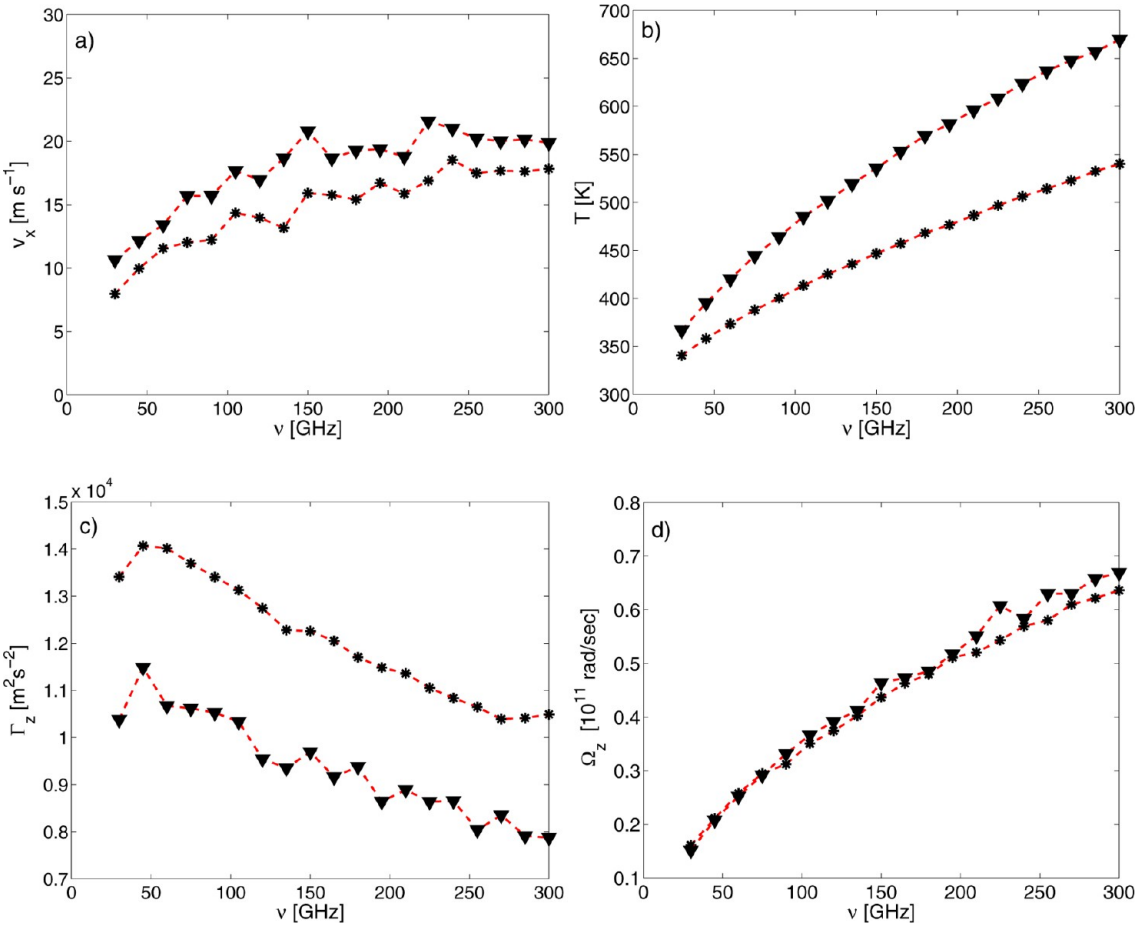

Figure 5. (a) Slip velocities of water confined between two graphene layers (*) and confined between graphene and β-cristobalite (▼). The electric field amplitude is fixed at E = 0.053 V Å^{-1}, and the frequency range is 30−300 GHz (horizontal axis). The same meaning of the symbols is adopted for the next three pictures. (b) Temperatures of water. (c) Specific torques. (d) Streaming angular velocities. Data in part (a) are taken at the bin N = 16 of the corresponding velocity profiles, close to graphene; the bin N = 50 (i.e., the bin in the center of the channel) has been considered for the data plotted in parts (b) and (c). Data of part (d) are averages of Ω_z values taken in the bin range of 25−75 (i.e., approximately the bulk region).

streaming angular velocity profiles showing a similarity with the symmetric channel. However, torques next to the β-cristobalite surface are different in shape owing to the strong hydrophilicity and corrugation of the surface.

Figure 4 (panels a and b) depicts the symmetric channel and the asymmetric channel equilibrium density profiles of water, respectively. When confined between two different surfaces (Figure 4b), the first peak close to graphene (left side of the channel) is higher than the first peak close to β-crostobalite, suggesting a higher surface-induced structural ordering close to graphene. Note that the surfaces are both rigid and β-cristobalite is more corrugated, owing to the silanol groups whose bO oxygens interact with water. Note that the density profiles evaluated when the field is switched on (not reported) are similar to the equilibrium density profiles. The density profiles for the symmetric and the asymmetric channels show that the effective channel width is different from the distance between the two graphene layers' center of mass separation, and the distance between graphene and the innermost bO layer of β-cristobalite center of mass, h = 2.57 nm. To evaluate the effective channel width for the symmetric channel, we subtract σ_{CO} [i.e., h_{eff} = 2.57 − (σ_{CO} + σ_{CO})/2 − 2.25 nm], since water is depleted at the interface. Similarly, for the asymmetric channel, we subtract out σ_{CO} and σ_{ObO} [i.e., h_{eff} = 2.57 − (σ_{CO} + σ_{ObO})/2 − 2.28 nm]. Note that in the velocity, temperature, torque, and angular velocity profiles of Figures 2 and 3, the horizontal axis (channel) width considered is $h' \lesssim h_{eff}$ (assumed equal for the symmetric and the asymmetric channel), to avoid the statistical noise in the bins immediately adjacent the interfaces.

Next, we study the symmetric and the asymmetric channel, fixing the REF frequency at ν = 20 GHz and considering eight REF amplitudes in the range of E = 0.011−0.16 V Å^{-1} (NEMD profile shapes are very similar to the previous case and are not plotted). An almost undetectable flow is present at E = 0.011 V Å^{-1}, the smallest field used in this work, which further gives an almost negligible temperature increase, torque, and angular velocity. The minimum REF amplitude yielding appreciable velocities and good signal-to-noise ratio, at least with our system size, is E = 0.032 V Å^{-1}. As expected for the symmetric channel, all the velocity profiles are symmetric with respect to the center of the channel, giving a zero net flow rate.

The temperature profiles in the range of 0.011−0.16 V Å^{-1} show that the fluid temperature monotonically increases, ranging from 300 to 350 K. The torque (eq 2) attains $\Gamma_z \sim 0.6 \times 10^4$ m^2 s^{-2} for E = 0.032 V Å^{-1} and $\Gamma_z \sim 3 \times 10^4$ m^2 s^{-2} for the highest E = 0.16 V Å^{-1}. The streaming angular velocity Ω_z increases as E increases, since higher amplitudes increase the speed at which the dipoles align with the REF.

The asymmetric channel NEMD results, for ν = 20 GHz and for the eight REF amplitudes in the range of E = 0.011−0.16 V

dx.doi.org/10.1021/la404805s | Langmuir 2014, 30, 3095−3109

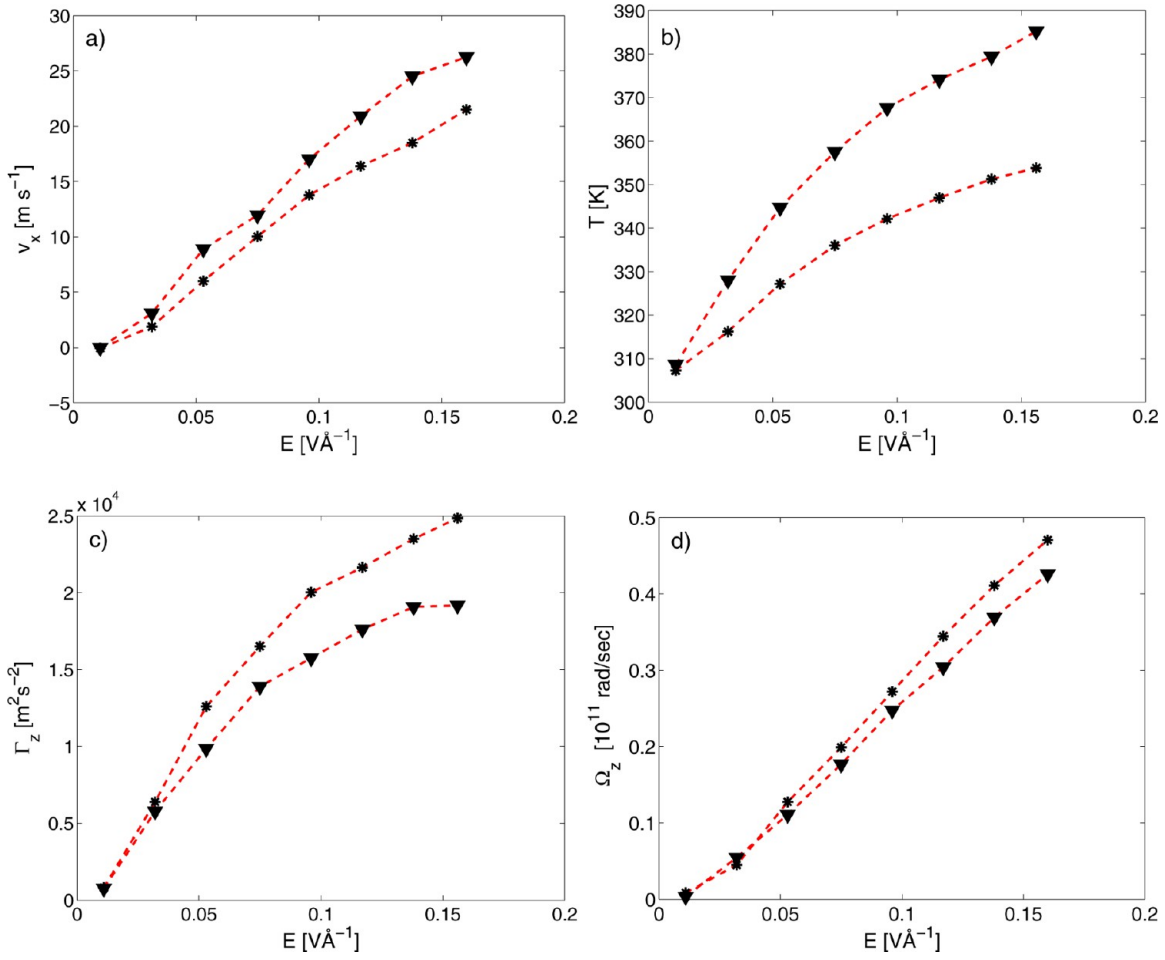

Figure 6. (a) Slip velocities of water confined between two graphene layers (*) and confined between graphene and β-cristobalite (▲). The electric field frequency is fixed at ν = 20 GHz, and the amplitude range is 0.011−0.16 V Å^{-1} (horizontal axis). The same meaning of the symbols is adopted for the next three pictures. (b) Temperatures of water. (c) Specific torques. (d) Streaming angular velocities. Data in part (a) are taken at the bin N = 16 of the corresponding velocity profiles, close to graphene; the bin N = 50 (i.e., the bin in the center of the channel) has been considered for the data plotted in parts (b and c); data of part (d) are averages of Ω_z values taken in the bin range of 25−75 (i.e., approximately the bulk region).

Å^{-1}, show that this channel can be exploited to pump water, there being a nonzero net flow rate. For the highest field E = 0.16 V Å^{-1}, a slip velocity of ∼25 ms^{-1} is achieved at the graphene interface. Again, the asymmetric channel temperatures are higher than the symmetric channel temperatures. The torque profiles evaluated in the center of the channel yield similar but lower values with respect to the symmetric channel. Angular velocities Ω_z are similar to the symmetric channel Ω_z profiles.

We note at this point that we have not considered two β-cristobalite surfaces as another symmetric channel since for h = 2.57 nm, the density profile shows almost no bulk region. We further comment on the choice ν = 20 GHz, which will also be used in the next section for the comparison with theory. The fluid velocity increases when the REF amplitude or frequency increases (neglecting saturation effects), but inevitably viscous stresses are increased by the stronger and more rapidly varying electric fields, heating up the fluid. One of the objectives of our investigation is to find the smallest REF amplitudes and frequencies, yielding appreciable velocities (i.e., higher flow productions under the asymmetric channel) concomitantly with moderate fluid heating, and ν = 20 GHz represents a good compromise. We further point out that in the next section, where the NEMD results are compared with the predictions of the theory, several transport coefficients are involved, which may depend on the temperature. With E = 0.032 V Å^{-1} and ν = 20 GHz, the fluid attains $v \sim 2$ ms^{-1} with T = 316 K, low enough to not complicate the estimations of the transport coefficients. Note that the rotational relaxation time of water (SPC/E) at T = 300 K is 7−10 ps,[50] corresponding to the frequency range of 16−23 GHz.

Figure 5 compares the symmetric and the asymmetric channel (i.e. overlapping Figure 2 and Figure 3 results), plotted as a function of frequency. Slip velocities are taken at the bin N = 16 of the corresponding velocity profiles, close to the graphene surface, and temperatures and torques at the central bin N = 50 (since these profiles are approximately flat in the bulk region). The Ω_z profiles are averaged between the bin N = 25 and N = 75, thus excluding the region next to the interfaces (i.e. in Figure 5d the angular velocity is calculated as $\sum_{n_i=25}^{75}(\Omega_{z,i})/51$, where $\Omega_{z,i}$ is the value at the bin N_i). Figure 5a illustrates that the asymmetric channel yields higher slip velocities than the symmetric channel and that in the range of 30−150 GHz, the velocity steadily increases as the frequency increases. In the range of 150−300 GHz, the velocity saturates toward $v \sim 20$ ms^{-1}, where the high temperatures tend to randomize the dipole orientations, and the permanent dipoles gradually lose their ability to keep up with the faster field

dx.doi.org/10.1021/la404805s | Langmuir 2014, 30, 3095−3109

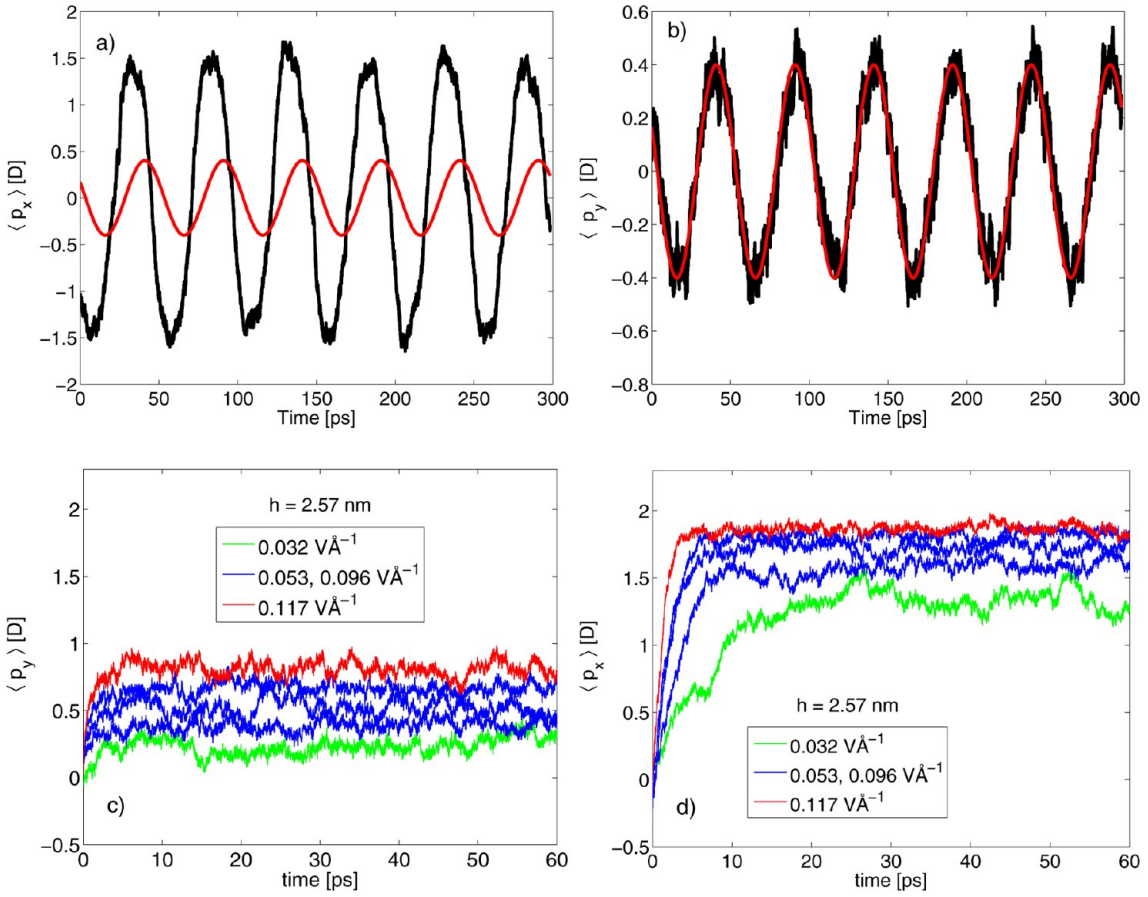

Figure 7. (a) The x component of the average net dipole moment of water confined between two graphene layers (black line) subjected to the rotating electric field $\mathbf{E} = E[\cos(2\pi\nu t), \sin(2\pi\nu t), 0]$, where $E = 0.0532$ V Å and $\nu = 20$ GHz (depicted in red). The amplitude of the field is divided by a constant factor, equal for both the (a and b) plots, for readability purposes. (b) The y component of the average net dipole moment of water (same E, ν). The angle brackets indicate averages over the total number of water molecules. Profiles are taken in the steady state. (c) Time-series of the y component of the average dipole moment $\langle p_y \rangle$ of water for the static electric field polarized in the y direction (perpendicular to the walls). The (symmetric) channel width is on the top of the legend and the field amplitudes are indicated inside the legend. (d) Time-series of the x component of the average dipole moment $\langle p_x \rangle$ of water for the static field polarized in the x direction (parallel to the walls).

rotations, reducing the rotational−translational coupling. Figure 5b illustrates that the symmetric channel fluid temperatures are lower than the asymmetric channel ones. As noticed, torques from the asymmetric channel are slightly lower than torques from the symmetric channel (see Figure 5c), which can be be ascribed to the higher temperatures obtained in the asymmetric channel (see Figure 5b). Figure 5d shows almost no dependence of Ω_z on the symmetry of the channel, at least in the averaged region.

Figure 6 collects the symmetric channel and the asymmetric channel results for the REF frequency fixed at $\nu = 20$ GHz and considering eight REF amplitudes in the range $E = 0.011$−0.16 V Å^{-1} (NEMD profile results not plotted). In Figure 6a, slip velocities almost linearly increase as the REF amplitude increases, with slightly higher asymmetric channel slip velocities. Temperatures (see Figure 6b) increase as the REF amplitude increases, and the trend is not linear since the dependence weakens for $E \gtrsim 0.07$ V Å^{-1}. Again, the symmetric channel temperatures are always smaller than the asymmetric channel temperatures. Torques, plotted in Figure 6c, increase as the REF amplitude increases with slightly smaller values for the asymmetric channel. Lastly, in Figure 6d, we observe an almost linear increase of Ω_z as the REF amplitude increases, with no significant differences between the asymmetric and the symmetric channel.

In view of the previous analysis, we now comment on a recent MD result which proposed that water without free charges can be pumped inside carbon nanotubes,[51] applying uniform static electric fields. This result was later argued to be due to an artifact of the simulation related to the simple cutoff scheme in GROMACS.[25] We have conducted simulations to investigate this problem, and we have found that if an axial (parallel to the x direction) uniform static electric field is applied on the fluid system, with the amplitudes taken in the range used in this work which are similar to the amplitudes used by Joseph and Aluru (i.e., $E = 0.01$ and 0.1 V Å^{-1}), no water flow is observed. We obtain $v = 0$ (eq 7) across the channel (with $\Gamma = 0$, $\Omega_z = 0$, and, as expected, $T \simeq 300$ K for both the symmetric and the asymmetric channels). This is in contrast with the conclusion of Joseph and Aluru,[51] who observed water flow in carbon nanotubes with uniform electric fields. Their result was explained in terms of the coupling between translational and rotational motion, which, when the orientation of water is maintained along the channel axis, yields a net water flux. We conducted the simulations in a planar geometry finding that there is no net flow. We also conducted NEMD simulations (at the same electric field amplitudes) on a

dx.doi.org/10.1021/la404805s | Langmuir 2014, 30, 3095−3109

(18,12) CNT (diameter of 2.05 nm) with a length of 5.53 nm and water density of 0.63 kg m^{-3},[52] yielding N_w = 395, without observing any flow. The CNT was initially filled with water, neglecting water permeation effects. Our results agree with the prediction of Bonthuis et al.[13] who, theoretically and with computer simulations, demonstrated that with static electric fields and in the absence of free charges it is not possible to pump water.

Figure 7a plots the x component of the average net dipole moment of water as a function of time, averaged over N_w (i.e., the quantity $\langle p_x(t)\rangle = \sum_i p_{i,x}(t)/N_w$ where the index i spans N_w) and sampled every 10 time steps in the steady state for 300 ps. The quantity is overlapped with the x component of the REF [i.e., $E\cos(2\pi\nu t)$] depicted in red and divided by a constant factor to match the amplitudes. Similarly, Figure 7b plots the y component, overlapped with $E\sin(2\pi\nu t)$ divided by the same factor. Fitting the net average dipole moment with $p_x = p_{0x}\cos(2\pi\nu t - \phi)$, where ϕ is the phase angle between E_x and p_x, shows that the dipole lags the field by $\phi/(2\pi\nu) \sim 6$ ps. Interestingly, for the dipole response in the y direction (i.e., perpendicular to the walls), we find a lag time $\phi/(2\pi\nu) \sim 0$, as can be seen in Figure 7b. This striking effect qualitatively agrees with the investigations of Zhang et al.,[53] who demonstrated that for confined liquids, the dielectric relaxation time of SPC/E water in the direction perpendicular to the graphene walls is much smaller than the relaxation time parallel to graphene. In our case, the y component of the average net dipole moment of water relaxes toward the instantaneous REF vector direction much faster than its relaxation in the x direction. We observe this effect also in the differences between Figure 7 (panels c and d) (to be explained), where static fields are used. Figure 7 (panels a and b) also shows that $p_x \approx 3p_y$, revealing a strong anisotropy in the polarization response of the fluid. These results will be used in the next section, where we compare our NEMD results with theory. Although interesting, a detailed analysis of the polarization response of highly confined water under REF is not the focus of our investigation and will be deferred to a future work.

COMPARISON WITH CONTINUUM THEORY

The ENS equations, including the spin angular momentum[15−18] with the geometry of Figure 1 (top left), read

$$\rho\frac{\partial v_x}{\partial t} = \rho F_e + (\eta_0 + \eta_r)\frac{\partial^2 v_x}{\partial y^2} - 2\eta_r\frac{\partial \Omega_z}{\partial y} \tag{14}$$

$$\rho\Theta\frac{\partial \Omega_z}{\partial t} = \rho\Gamma_z + 2\eta_r\left(\frac{\partial v_x}{\partial y} - 2\Omega_z\right) + \zeta\frac{\partial^2 \Omega_z}{\partial y^2} \tag{15}$$

where ρ is the fluid density, η_0 the shear viscosity, η_r the vortex viscosity, and $\zeta = \zeta_0 + \zeta_r$ and Θ are the equivalent spin viscosities and the scalar moment of inertia per unit mass of water, respectively, assuming that the liquid is isotropic. F_e is the external force (zero here, since no gravity-like forces are applied) and Γ_z the torque per unit mass exerted by the REF on water molecules. The term v_x is the streaming velocity in the x direction and Ω_z the streaming angular velocity in the z direction.

We compare our NEMD velocity profile with the ENS analytical solution, including REF[13,14] for the symmetric channel (two equal graphene sheets separated by h = 2.57 nm), solving for the fluid velocity $v_x(y)$. The ENS mathematical boundaries are placed at $l = \pm 1.05$ nm with respect to the center of the channel (placed at $y = 0$), with $|l| < h/2$ to take into account the excluded volume next to the interface due to the depletion layer. The classical BC for the velocity and the angular velocity are

$$\pm b\frac{\partial v_x}{\partial y}\Big|_{\mp l} = v_x|_{\mp l} \tag{16}$$

$$\pm s\frac{\partial \Omega_z}{\partial y}\Big|_{\mp l} = \Omega_z|_{\mp l} \tag{17}$$

where b is the slip length and s the spin slip length,[54] both treated as free parameters in the symmetric problem[14] and here fixed a posteriori (to optimize agreement between ENS predictions and NEMD results) to the values of b = 20 nm and s = 0.3 nm. It should be pointed out that the slip length of water on graphene has been estimated by Kannam et al.[6] using an equilibrium MD procedure,[24] finding b = 60 nm. However, Kannam et al. and our estimates are not expected to be equal for three reasons: (1) the carbon structure in the work of Kannam et al. was vibrating and modeled with a complex potential, whereas our graphene is rigid and modeled with a simpler potential; (2) a flexible three-site SPC/Fw[55] water model was used by Kannam et al., and (3) the VP thermostatting scheme adds a modest degree of hydrophilicity to the graphene surface, which was not the case in the system of Kannam et al. (see De Luca et al. for details[31]). Although we have considered in this work b = 20 nm, we point out that larger values of b give similar results (but not smaller values).

We make use of the two quantities[14]

$$\chi = \rho\alpha E^2\nu\tau/[\eta_0(1 + \nu^2\tau^2)] \tag{18}$$

$$\kappa^2 = 4\eta_0\eta_r/[\zeta(\eta_0 + \eta_r)] \tag{19}$$

to be inserted in the solution for the streaming velocity

$$\begin{aligned} v_x(y) = {} & \{\chi[(kb\cosh(\kappa l) + \sinh(\kappa l))y - (b + l)\sinh(\kappa y)]\} \\ & /\{2[\kappa(b + l)(\cosh(\kappa l) + s\kappa\sinh(\kappa l)) \\ & + (\eta_r/\eta_0)(\kappa l\cosh(\kappa l) - \sinh(\kappa l) + (b + l)\kappa^2 s \\ & \sinh(\kappa l))]\} \end{aligned} \tag{20}$$

which, except for a minor change in the nomenclature, is the ENS solution derived by Bonthuis et al.[14] The field, E = 0.032 V $Å^{-1}$, and frequency, ν = 20 GHz, are used in eq 18 and in our NEMD simulations, where water reaches a temperature of T = 316 K. The vortex viscosity η_r can be estimated from

$$\eta_r = \frac{\rho\Gamma_z}{2}\frac{1}{\left(2\Omega_z - \frac{\partial u_x}{\partial y}\right)} \tag{21}$$

obtained by solving eq 15 for η_r in the steady state (i.e., $\partial\Omega_z/\partial t = 0$) in the limit of small spin diffusion term, i.e., $\zeta\partial^2\Omega_z/\partial y^2 \simeq 0$. From the NEMD velocity profile (not shown), torque (Figure 6c) and angular velocity (Figure 6d) we find the strain rate $\partial v_x/\partial y = 0.34 \times 10^{10}$ s^{-1}, $\Gamma_z = 0.62 \times 10^4$ m^2 s^{-2}, and $\Omega_z = 0.05 \times 10^{11}$ rad/s, respectively, yielding $\eta_r = 4.7 \times 10^{-4}$ Pa s, which is comparable to $\eta_r = 1.7 \times 10^{-4}$ Pa s[19] evaluated for SPC/Fw. We treat the spin viscosity ζ as an adjustable parameter, since there is no available estimate for SPC/E, setting $\zeta = 0.6 \times 10^{-21}$ kg m s^{-1} to optimize the agreement between theory and NEMD.[19] The shear viscosity is fixed at $\eta_0 = 5 \times 10^{-4}$ Pa s^{-1}[43] computed for SPC/E at T = 316 K.

dx.doi.org/10.1021/la404805s | Langmuir 2014, 30, 3095−3109

Table 1. Temperature, Torque, Streaming Angular Velocity, Strain Rate, Vortex, and Shear Viscosity for the Graphene−Graphene Channel, with Varying Electric Field Amplitude (First Column) and Fixed ν = 20 GHz and h = 2.57 nm[a]

E (V Å^{-1})	T (K)	Γ_z (10^4 m^2 s^{-2})	Ω_z (10^{11} rad s^{-1})	$\partial u_x/\partial y$ (10^{10} s^{-1})	η_r (10^{-4} Pa s)	η_0 (10^{-4} Pa s)
0.032	316	0.62	0.05	0.34	4.7	5.0
0.053	327	1.26	0.13	0.71	3.43	4.2
0.075	336	1.65	0.20	1.08	2.85	3.9
0.096	342	2.00	0.27	1.50	2.54	3.7
0.117	347	2.16	0.34	1.79	2.12	3.6

[a]The values of η_0 have been extracted from Markesteijn et al.[43]

Table 2. Polarizabilities Per Unit Mass $\alpha_\perp$, $\alpha_\parallel$, α, and Dipolar Relaxation Times $\tau_\perp$, $\tau_\parallel$, τ for the Graphene−Graphene Channel with Varying Static Electric Field Amplitude (First Column) and Fixed Wall Separation of h = 2.57 nm

E (V Å^{-1})	$\alpha_\perp$ (10^6 m^2 eV^{-1} kg^{-1})	$\tau_\perp$ (ps)	$\alpha_\parallel$ (10^6 m^2 eV^{-1} kg^{-1})	$\tau_\parallel$ (ps)	α (10^6 m^2 eV^{-1} kg^{-1})	τ (ps)
0.032	0.5	1	3	6.5	1.75	3.7
0.053	0.5	0.8	2.1	3.6	1.3	2.2
0.075	0.49	0.7	1.6	2.3	1.05	1.5
0.096	0.48	0.6	1.3	1.8	0.89	1.2
0.117	0.48	0.6	1.1	1.5	0.79	1.1

Estimates of Γ_z, Ω_z, $\partial v_x/\partial y$ (hence η_r) and η_0 are listed in the first row of Table 1, for E = 0.032 V Å^{-1}. Table 1 also includes data for the amplitudes 0.053, 0.075, 0.096, 0.117 V Å^{-1} used later, where it can be seen that the vortex viscosity decreases when the fluid temperature increases.

The polarizability per unit mass α = 3.3 × 10^6 m^2 eV^{-1} kg^{-1} and the dipolar relaxation time τ = 7 ps of SPC/E water (eq 18) were estimated by Bonthuis et al.,[14] by applying a static electric field of magnitude 0.01 V Å^{-1}. With our E = 0.011 V Å^{-1} (and ν = 20 GHz for h = 2.57 nm), we obtain $v_x(y) \approx 0$ across the channel (not shown). The larger E = 0.032 V Å^{-1} enables slip velocities 1−10 ms^{-1} for $N_w \approx 300$ and simulation times ≈10 ns. Following the procedure of Bonthuis et al.,[14] we estimate α and τ since we apply a larger field. Moreover, we explicitly account for the anisotropic polarization response of water induced by the spatial confinement in the y direction. Figure 7 (panels a and b), which was for the REF field E = 0.0532 VÅ and ν = 20 GHz, showed that the amplitude of the dipole response orthogonal to the walls (the projection of the average net dipole moment of water in the y axis) was smaller than the amplitude of the parallel response (projection of the average net dipole moment of water in the x axis). On the basis of this result, we assume that there exists an orthogonal $\alpha_\perp$ and parallel component $\alpha_\parallel$ such that α (to be inserted in eq 18) is the arithmetic average

$$\alpha = \frac{\alpha_\perp + \alpha_\parallel}{2} \tag{22}$$

where $\alpha_\perp$ is computed, applying a uniform static electric field polarized in the y direction (i.e., $\mathbf{E}_\perp = E_\perp \hat{\mathbf{y}}$) and $\alpha_\parallel$ is computed applying $\mathbf{E}_\parallel = E_\parallel \hat{\mathbf{x}}$ and tracing in both cases the fluid polarization response. Likewise, we assume that τ is the arithmetic average of its orthogonal $\tau_\perp$ and parallel $\tau_\parallel$ components

$$\tau = \frac{\tau_\perp + \tau_\parallel}{2} \tag{23}$$

measured by applying the same $\mathbf{E}_\perp$ and $\mathbf{E}_\parallel$, respectively.

The equation for the dielectric relaxation is to a first approximation given by refs 16 and 19 as

$$\frac{d\mathbf{p}}{dt} = \frac{\alpha\mathbf{E} - \mathbf{p}}{\tau} \tag{24}$$

where the average net dipole moment of water is $\mathbf{p} = \mathbf{M}(t)/N_w = \sum_{i=1}^{N_w} \boldsymbol{\mu}_i(t)/N_w$, $\boldsymbol{\mu}_i$ is the dipole moment of SPC/E (μ = 2.35 D), and $\mathbf{M}$ is the total dipole moment. Integrating eq 24 for orthogonal fields, if $p_\perp$ = 0 at t = 0 (i.e., neglecting surface effects and assuming unpolarized fluid at $E_\perp$ = 0) gives

$$p_\perp(t) = \alpha_\perp E_\perp (1 - e^{-t/\tau_\perp}) \tag{25}$$

Fitting the NEMD time-series of $p_\perp(t) = M_\perp(t)/N_w$ (see Figure 7c, green line) with eq 25 provides the estimate $\alpha_\perp$ = 0.5 × 10^6 m^2 eV^{-1} kg^{-1} and $\tau_\perp$ = 1 ps. For the parallel direction, fitting $p_\parallel(t) = M_\parallel(t)/N_w$ (Figure 7d, green line) with $p_\parallel(t) = \alpha_\parallel E_\parallel[1 - e^{(-t/\tau_\parallel)}]$ gives $\alpha_\parallel$ = 3 × 10^6 m^2 eV^{-1} kg^{-1} and $\tau_\parallel$ = 6.5 ps. Thus, α = 1.75 × 10^6 m^2 eV^{-1} kg^{-1} and τ = 3.7 ps (eqs 22 and 23). Table 2 lists α and τ for E = 0.032−0.117 V Å^{-1} (to be used later) and their parallel and orthogonal components, where it can be seen $\alpha_\perp < \alpha_\parallel$ and $\tau_\perp < \tau_\parallel$ for every E owing to the confinement. We point out that the fields $E_\perp$, $E_\parallel$, and the fields in eqs 2,4, and 9 are effective fields assumed to coincide with the external electric field; that is, we neglect the screening effect of water molecules. Moreover, we assume that the walls are transparent to the electric field. We emphasize that our $\alpha_\parallel$ and $\tau_\parallel$ are almost equal to the estimates of Bonthuis et al.,[14] revealing that we are still approximately in the linear regime, although unavoidably α = 1.75 × 10^6 < 3.3 × 10^6 m^2 eV^{-1} kg^{-1} and τ = 3.7 < 7 ps, owing to the confinement effects. Also, the onset of nonlinear effects takes place in the range of $E \gtrsim 0.032$ V Å^{-1}, as can be seen in Figure 6c, where Γ_z does not quadratically depend on E, as it would in the linear regime,[14] and can be seen in the trend of Figure 7d where the average net dipole moment of water as a function of E gradually saturates, reaching ∼18 D at the highest field. Note that in the linear regime, the induced dipole moment is proportional to the applied field E[56] (i.e., the relation $\mathbf{p} = \alpha\mathbf{E}$ with constant α is valid). However, the decrease of $\alpha_\parallel$ in Table 2 as the field increases from $E \sim$ 0.05 V Å^{-1} is a further indication of saturation effects emerging in this range.

Note that Sutmann[57] found that at E = 0.1 V Å^{-1}, the orientation of the average dipole moment $\mathbf{p}$ of water in the (static) field direction $\mathbf{E}$ is $\cos(\mathbf{p}\cdot\mathbf{E})$ = 0.81, which, given that μ

dx.doi.org/10.1021/la404805s | Langmuir 2014, 30, 3095−3109

= 1.98 D in their specific case, yields an average net dipole moment 1.6D (at T = 300 K), in good accord with our result in Figure 7d; that is, $\langle p_x \rangle \sim 1.8$ D obtained for $E = 0.11$ V Å^{-1}, red profile. The author also showed that the polarization density of water as a function of the external field amplitude starts to deviate from a straight line at $E \approx 0.025$ V Å^{-1}, which reasonably agrees with our deviations from the linear regime appearing at $E \gtrsim 0.032$ V Å^{-1}, although they used a flexible model for water. With a rigid water model, dielectric saturation effects have been detected starting from $E \approx 0.04$ V Å^{-1}.[58]

After estimating χ and κ^2, we compare the ENS predictions (including REF) plotting eq 20 (black line) and our NEMD streaming velocity profile (red points) in Figure 8 (top).

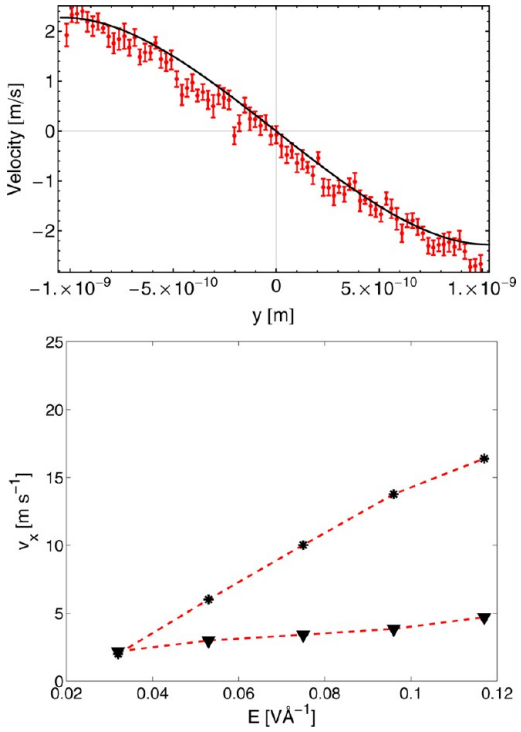

Figure 8. (top) Analytical solution for the velocity of the ENS equations relative to the symmetric channel (black line) compared with NEMD simulation results (red ●) for $E = 0.032$ V Å^{-1}, $\nu = 20.0$ GHz, and $h = 2.57$ nm. Note that the edges of the x axis, $\pm l$, are determined from $l \simeq \pm (h - \sigma_{CO})/2$, as explained in the text. The error bars represent the standard errors computed from nine independent simulations. (bottom) NEMD slip velocity (*) evaluated at the bin N = 16 (which is close to the interface) of the streaming velocity profile compared with the ENS analytical solution for the velocity computed at the boundary (▼) for the symmetric channel (two equal graphene walls). The channel width is fixed at $h = 2.57$ nm and $\nu = 20.0$ GHz, whereas the field amplitude varies on the horizontal axis in the range of 0.032−0.117 V Å^{-1}.

Excellent agreement is found. Note that eq 20 predicts $v_x \sim 2$ ms^{-1} at $y = -|l|$ (i.e., the slip velocity close to the left side of the channel) and NEMD gives the same value at the bin N = 16. Figure 8 (bottom) compares the theory and the NEMD predictions for the REF amplitude range of 0.032−0.117 V Å^{-1}; that is, we plot $v_x(-|l|)$ and the NEMD slip velocities (at the bin N = 16) as a function of the REF amplitude. The coefficients needed to compute χ and κ^2 are collected in Tables 1 and 2 and obtained by iterating the procedure outlined before. It can be seen that as the REF strength increases from 0.032 to 0.117 V Å^{-1}, the theoretical prediction gradually diverges from the NEMD results, since, as explained, we enter into the nonlinear regime when saturation effects become important. The largest difference is detectable for the largest field strength $E = 0.117$ V Å^{-1}, where eq 20 predicts $\nu \sim 5$ ms^{-1} while the NEMD result gives $\nu \sim 15$ ms^{-1}. Note that adjusting ζ does not substantially improve the agreement between theory and NEMD in the range of $E = 0.053$−0.117 V Å^{-1}, so it is not just an issue with an adjustable free parameter. Our results suggest that the hydrodynamic theory, which was developed assuming the system remains in the linear regime, should be refined to include nonlinearities arising with stronger fields.

CONCLUSION

We have quantitatively compared our NEMD results with the predictions of the extended Navier−Stokes equations, including the effect of an external spatially uniform rotating electric field,[14] showing excellent agreement. The translational−rotational coupling is responsible for the conversion of the streaming spin angular momentum, induced by the external rotating field, to translational linear momentum. The conversion can be exploited to achieve noncontact pumping of water at the nanoscale, if water is confined between surfaces with different degrees of hydrophobicity.

Simulations have been carried out for experimentally achievable conditions. A slab of (111) β-cristobalite represents the hydrophilic side of the planar nanochannel, reproducing almost exactly the stick velocity boundary condition (i.e., $\nu \sim 0$) at the interface. A graphene sheet is placed on the opposing hydrophobic side of the channel. The pumping efficiency is very sensitive to the parameters of the external electric field. We have explored the amplitude range of 0.011−0.16 V Å^{-1} in conjunction with frequencies spanning the range of 20−300 GHz for wall center of mass separation ∼2.5 nm and ∼300 water molecules. For all but the smallest field of 0.011 V Å^{-1}, we have found significant fluid velocities of the order 1−20 ms^{-1} and reasonably low temperatures for $\nu \lesssim 40$ GHz, confirming that this electrokinetic flow can be efficiently exploited as a promising alternative method to pump water at the nanoscale. Particularly interesting for nanofluidic applications are field amplitudes ∼0.03 V Å^{-1} and frequencies ranging in a small window of the microwave region around ∼20 GHz, which approximately corresponds to the inverse of the dipolar relaxation time of water. In that region, velocities of the order of ∼2 ms^{-1} are attained, concomitantly with moderate heating of water, where T = 316 K in the steady state. Note that in our thermostatting strategy, the fluid is not directly coupled with a thermostat and that the heat flux is naturally conducted from the fluid to the walls, as in a real experiment. The electric field with amplitude 0.032 V Å^{-1} and frequency 20 GHz is also employed to compare our NEMD streaming velocity profile result with the prediction of the analytical solution of the ENS equations solved for the velocity. The agreement is excellent, however, for higher field strengths nonlinear effects take place, and the matching is less accurate since the theory derived by Bonthuis et al.[14] was developed assuming the system remains in the linear regime.

Two comments are in order regarding the comparison between theory and NEMD results: (1) the strong anisotropy of the polarization response of water induced by the confinement has been taken into account considering two water polarizabilities and two dielectric relaxation times for water, one for the direction perpendicular to the walls, and the

dx.doi.org/10.1021/la404805s | Langmuir 2014, 30, 3095−3109

other for the parallel direction and (2) the spin viscosity required in the ENS equations has been treated as an adjustable parameter since no estimate is available in the literature for SPC/E. This was set to optimize the match with the theory (i.e., $\zeta = 0.6 \times 10^{-21}$ kg m s^{-1}). This value is comparable with $\zeta = 1.6 \times 10^{-21}$ kg m s^{-1} estimated for a flexible water model at $T = 319$ K by Hansen et al.[19]

Finally, we point out that in a real experiment the dielectric screening of the walls may also be significant (the dielectric constant of β-cristobalite is 4.5[59] and of graphene is in the range 4−16.[60]). However, low permittivity materials should allow enough passage of electric field such that the conversion remains efficient.

Future investigations should focus not only on the study of larger systems, to scrutinize the details of the streaming velocity and streaming angular velocity close to interfaces, but also on the study of systems with different geometries like carbon nanotubes and on the energy efficiency of this method, compared for example with the standard pressure-driven flow. Moreover, our results suggest that the theory may be extended to include nonlinear effects arising at higher field strengths. In this work, we have left out the interesting analysis of the anisotropic polarization response of highly confined water subjected to an external rotating electric field, which may further contribute to the understanding of the complex behavior of water close to the hydrophilic and hydrophobic surfaces.

AUTHOR INFORMATION

Corresponding Author

*E-mail: btodd@swin.edu.au.

Notes

The authors declare no competing financial interest.

ACKNOWLEDGMENTS

Computational resources were provided by the Swinburne Supercomputer Centre, the Victorian Partnership for Advanced Computing HPC Facility and Support Services, and an award under the Merit Allocation Scheme on the NCI National Facility at the Australian National University. J.S.H. wishes to acknowledge Lundbeckfonden for supporting this work as a part of Grant R49-A5634. We thank Professor Mike Allen for valuable discussions and for helping in the literature review.

REFERENCES

(1) Mishra, A. K.; Ramaprabhu, S. Functionalized graphene sheets for arsenic removal and desalination of sea water. *Desalination* **2011**, *282*, 39−45.

(2) Cohen-Tanugi, D.; Grossman, J. C. Water desalination across nanoporous graphene. *Nano Lett.* **2012**, *12*, 3602−3608.

(3) Young, E. W. K.; Beebe, D. J. Fundamentals of microfluidic cell culture in controlled microenvironments. *Chem. Soc. Rev.* **2010**, *39*, 1036−1048.

(4) Hummer, G.; Rasaiah, J. C.; Noworyta, J. P. Water conduction through the hydrophobic channel of a carbon nanotube. *Nature* **2001**, *414*, 188−190.

(5) Kannam, S. K.; Todd, B. D.; Hansen, J. S.; Daivis, P. J. How fast does water flow in carbon nanotubes ? *J. Chem. Phys.* **2013**, *138*, 094701−094710.

(6) Kannam, S. K.; Todd, B. D.; Hansen, J. S.; Daivis, P. J. Slip length of water on graphene: Limitations of non-equilibrium molecular dynamics simulations. *J. Chem. Phys.* **2012**, *136*, 024705−0247014.

(7) Bruus, H. *Theoretical Microfluidics*; Oxford University Press: Oxford, 2008.

(8) Ajdari, A.; Bocquet, L. Giant amplification of interfacially driven transport by hydrodynamic slip: Diffusio-osmosis and beyond. *Phys. Rev. Lett.* **2006**, *96*, 186102−186106.

(9) Qiu, H.; Shen, R.; Guo, W. Vibrating carbon nanotubes as water pumps. *Nano Res.* **2011**, *4*, 284−289.

(10) Longhurst, M. J.; Quirke, N. Temperature-driven pumping of fluid through single-walled carbon nanotubes. *Nano Lett.* **2007**, *7*, 3324−3328.

(11) Gong, X. J.; Li, J. Y.; Lu, H. J.; Wan, R. Z.; Li, J. C.; Hu, J.; Fang, H. P. A charge-driven molecular water pump. *Nat. Nano* **2007**, *2*, 709−712.

(12) Rinne, K. F.; Gekle, S.; Bonthuis, D. J.; Netz, R. R. Nanoscale pumping of water by AC electric fields. *Nano Lett.* **2012**, *12*, 1780−1783.

(13) Bonthuis, D. J.; Horinek, D.; Bocquet, L.; Netz, R. R. Electrohydraulic power conversion in planar nanochannels. *Phys. Rev. Lett.* **2009**, *103*, 144503−144507.

(14) Bonthuis, D. J.; Horinek, D.; Bocquet, L.; Netz, R. R. Electrokinetics at aqueous interfaces without mobile charges. *Langmuir* **2010**, *26*, 12614−12625.

(15) Evans, D. J.; Streett, W. B. Transport properties of homonuclear diatomics II. Dense fluids. *Mol. Phys.* **1978**, *36*, 161−176.

(16) de Groot, S. R.; Mazur, P. *Non-Equilibrium Thermodynamics*; Dover: Mineola, NY, 1984.

(17) Snider, R. F.; Lewchuk, K. S. Irreversible thermodynamics of a fluid system with spin. *J. Chem. Phys.* **1967**, *46*, 3163−3172.

(18) Condiff, D.; Dahler, J. Fluid mechanical aspects of antisymmetric stress. *Phys. Fluids* **1964**, *6*, 842−855.

(19) Hansen, J. S.; Bruus, H.; Todd, B. D.; Daivis, P. J. Rotational and spin viscosities of water: Application to nanofluidics. *J. Chem. Phys.* **2010**, *133*, 144906−144913.

(20) Hansen, J. S.; Dyre, J. C.; Daivis, P. J.; Todd, B. D.; Bruus, H. Nanoflow hydrodynamics. *Phys. Rev. E* **2011**, *84*, 036311−036317.

(21) Felderhof, B. U. Ferrohydrodynamic pumping of a ferrofluid or electrohydrodynamic pumping of a polar liquid through a planar duct. *Phys. Fluids* **2011**, *23*, 092002−092008.

(22) Hansen, J. S.; Daivis, P. J.; Todd, B. D. Molecular spin in nano-confined fluidic flows. *Microfluid. Nanofluid.* **2009**, *6*, 785−795.

(23) Hansen, J. S.; Daivis, P. J.; Todd, B. D. Viscous properties of isotropic fluids composed of linear molecules: Departure from the classical Navier-Stokes theory in nano-confined geometries. *Phys. Rev. E* **2009**, *80*, 046322−046331.

(24) Hansen, J. S.; Todd, B. D.; Daivis, P. J. Prediction of fluid velocity slip at solid surfaces. *Phys. Rev. E* **2011**, *84*, 016313−016231.

(25) Bonthuis, D. J.; Falk, K.; Kaplan, C. N.; Horinek, D.; Berker, A. N.; Bocquet, L.; Netz, R. R. Comment on "Pumping of confined water in carbon nanotubes by rotation-translation coupling". *Phys. Rev. Lett.* **2010**, *105*, 209401.

(26) De Luca, S.; Todd, B. D.; Hansen, J. S.; Daivis, P. J. Electropumping of water with rotating electric fields. *J. Chem. Phys.* **2013**, *138*, 154712−154722.

(27) Swainson, I. P.; Dove, M. T. Molecular dynamics simulation of α- and β-cristobalite. *J. Phys.: Condens. Matter* **1995**, *7*, 1771−1788.

(28) Puibasset, J.; Pellenq, R. J.-M. Grand canonical Monte Carlo simulation study of water structure on hydrophilic mesoporous and plane silica substrates. *J. Chem. Phys.* **2003**, *119*, 9226−9233.

(29) Argyris, D.; Tummala, N. R.; Striolo, A.; Cole, D. R. Molecular structure and dynamics in thin water films at the silica and graphite surfaces. *J. Phys. Chem. C* **2008**, *112*, 13587−13599.

(30) Zhuravlev, L. T. The surface chemistry of amorphous silica. *Colloids Surf.* **2000**, *173*, 1−38.

(31) De Luca, S.; Todd, B. D.; Hansen, J. S.; Daivis, P. J. A new and effective method for thermostatting confined fluids. *J. Chem. Phys.* **2014**, *140*, 054502−054515.

(32) Bernardi, S.; Todd, B. D.; Searles, D. J. Thermostating highly confined fluids. *J. Chem. Phys.* **2010**, *132*, 244706−244716.

(33) Berendsen, H. J. C.; Grigera, J. R.; Straatsma, T. P. The missing term in effective pair potentials. *J. Phys. Chem.* **1987**, *91*, 6269−6271.

(34) Novoselov, K. S.; Geim, A. K.; Morozov, S. V.; Jiang, D.; Zhang, Y.; Dubonos, S. V.; Grigorieva, I. V.; Firsov, A. A. Electric field effect in atomically thin carbon films. *Science* **2004**, *306*, 666−669.
(35) Werder, T.; Walther, J. H.; Jaffe, R. L.; Halicioglu, T.; Koumoutsakos, P. On the water-carbon interaction for use in molecular dynamics simulations of graphite and carbon nanotubes. *J. Phys. Chem. B* **2003**, *107*, 1345−1352.
(36) Fan, X. F.; Zheng, W. T.; Chihaia, V.; Shen, Z. X.; Kuo, J.-L. Interaction between graphene and the surface of SiO_2. *J. Phys.: Condens. Matter* **2012**, *24*, 305004−305014.
(37) Ciccotti, G.; Ferrario, M.; Ryckaert, J. P. Molecular dynamics of rigid systems in cartesian coordinates A general formulation. *Mol. Phys.* **1982**, *47*, 1253−1264.
(38) Badyal, Y. S.; Saboungi, M. L.; Price, D. L.; Shastri, S. D.; Haeffner, D. R.; Soper, A. K. Electron distribution in water. *J. Chem. Phys.* **2000**, *112*, 9206−9209.
(39) Wolf, D.; Keblinski, P.; Phillpot, S. R.; Eggebrecht, J. Exact method for the simulation of Coulombic systems by spherically truncated, pairwise r^{-1} summation. *J. Chem. Phys.* **1999**, *110*, 8254−8283.
(40) Takahashi, K.; Narumi, T.; Yasuoka, K. Cutoff radius effect of the isotropic periodic sum and Wolf method in liquid-vapor interfaces of water. *J. Chem. Phys.* **2011**, *134*, 174112−174119.
(41) Hansen, J. S.; Schroder, T. B.; Dyre, J. Simplistic coulomb forces in molecular dynamics: Comparing the Wolf and shifted-force approximations. *J. Phys. Chem. B* **2012**, *116*, 5738−5743.
(42) Raabe, G.; Sadus, R. J. Molecular dynamics simulation of the effect of bond flexibility on the transport properties of water. *J. Chem. Phys.* **2012**, *137*, 104512−104520.
(43) Markesteijn, A. P.; Hartkamp, R.; Luding, S.; Westerweel, J. A comparison of the value of viscosity for several water models using Poiseuille flow in a nano-channel. *J. Chem. Phys.* **2012**, *136*, 134104−134112.
(44) English, N. J.; MacElroy, J. M. D. Molecular dynamics simulations of microwave heating of water. *J. Chem. Phys.* **2003**, *118*, 1589−1593.
(45) Tanaka, M.; Sato, M. Microwave heating of water, ice and saline solution: Molecular dynamics study. *J. Chem. Phys.* **2007**, *126*, 034509−034518.
(46) Allen, M. P.; Tildesley, T. J. *Computer Simulation of Liquids*; Clarendon Press: Oxford, 1987.
(47) Travis, K. P.; Daivis, P. J.; Evans, D. J. Computer simulation algorithms for molecules undergoing planar Couette flow: A nonequilibrium molecular dynamics study. *J. Chem. Phys.* **1995**, *103*, 1109−1119.
(48) Travis, K. P.; Daivis, P. J.; Evans, D. J. Thermostats for molecular fluids undergoing shear flow: Application to liquid chlorine. *J. Chem. Phys.* **1995**, *103*, 10638−10652.
(49) Travis, K. P.; Daivis, P. J.; Evans, D. J. Erratum: Thermostats for molecular fluids undergoing shear flow: Application to liquid chlorine [J. Chem. Phys. 103, 10638 (1995)]. *J. Chem. Phys.* **1996**, *105*, 3893−3894.
(50) van der Spoel, D.; van Maaren, P. J.; Berendsen, H. J. C. A systematic study of water models for molecular simulation: Derivation of water models optimized for use with a reaction field. *J. Chem. Phys.* **1998**, *108*, 10220−10231.
(51) Joseph, S.; Aluru, N. R. Pumping of confined water in carbon nanotubes by rotation-translation coupling. *Phys. Rev. Lett.* **2008**, *101*, 064502−064506.
(52) Alexiadis, A.; Kassinos, S. Influence of water model and nanotube rigidity on the density of water in carbon nanotubes. *Chem. Eng. Sci.* **2008**, *63*, 2793−2797.
(53) Zhang, C.; Gygi, F.; Galli, G. Strongly anisotropic dielectric relaxation of water at the nanoscale. *J. Phys. Chem. Lett.* **2013**, *4*, 2477−2481.
(54) Hynes, J.; Kapral, R.; Weinberg, M. Particle rotation and translation in a fluid with spin. *Physica A* **1977**, *87*, 427−452.
(55) Wu, Y.; Tepper, H. L.; Voth, G. A. Flexible simple point-charge water model with improved liquid-state properties. *J. Chem. Phys.* **2006**, *124*, 024503−024515.
(56) Böttcher, C. J. F. *Theory of Electric Polarization: Dielectrics in static fields*, 2nd ed.; Elsevier: Amsterdam, 1993.
(57) Sutmann, G. Structure formation and dynamics of water in strong external electric fields. *J. Electroanal. Chem.* **1998**, *450*, 289−302.
(58) Alper, H. E.; Levy, R. M. Computer simulations of the dielectric properties of water: Studies of the simple point charge and transferrable intermolecular potential models. *J. Chem. Phys.* **1989**, *91*, 1242−1252.
(59) Shi, N.; Ramprasad, R. Atomic-scale dielectric permittivity profiles in slabs and multilayers. *Phys. Rev. B* **2006**, *74*, 045318−045324.
(60) Santos, E. J. G.; Kaxiras, E. Electric-field dependence of the effective dielectric constant in graphene. *Nano Lett.* **2013**, *13*, 898−902.